# Experimental Investigation of Thermal Ablation by Melting in a Hypersonic Shock Tunnel

Flavien Denis, Robert Hruschka, Myriam Bastide, Berthold Sauerwein, Yannick Hoarau, Robert Mose

# Experimental Investigation of Thermal Ablation by Melting in a Hypersonic Shock Tunnel

Flavien DENIS *, Robert HRUSCHKA †, Myriam BASTIDE ‡ and Berthold SAUERWEIN§
*French-German Research Institute of Saint-Louis, Saint-Louis, 68300, France*

Yannick HOARAU ¶, Robert MOSE ‖
*Strasbourg University, Strasbourg, 67081, France*

**In this paper a novel approach for the experimental measurement of the ablation by melting is presented. The experiments are carried out with a hypersonic shock tunnel. The tested models are made of gallium, which melts at low temperatures, allowing the generation and then the measurement of the ablation profiles within only two milliseconds. By means of an optical visualization, the model surface changes are recorded during the experiment. An image post-processing algorithm computes the ablation profiles. The results for two hemisphere-cone models and one hemisphere-cylinder model in a Mach 4.5 nitrogen flow are presented. It is found that the maximum ablation occurs at an angular position of around 30 degrees off-axis rather than at the stagnation point. This is most likely a consequence of the laminar-turbulent transition on the model forebody.**

## Nomenclature

| | | |
|---|---|---|
| $Cp$ | = | Heat capacity at constant pressure $[J \cdot kg^{-1} \cdot K^{-1}]$ |
| $d$ | = | Surface displacement $[mm]$ |
| $h$ | = | Enthalpy $[J \cdot kg^{-1}]$ |
| $\Delta H_f$ | = | Latent heat of fusion $[J \cdot kg^{-1}]$ |
| $M$ | = | Mach number $[-]$ |
| $P$ | = | Pressure $[Pa]$ or Power flux $[W \cdot m^{-2}]$ |
| $Re$ | = | Reynolds number $[-]$ |
| $Re/x$ | = | Reynolds number per meter $[m^{-1}]$ |

*Ph.D. Student, Aerodynamics, Measurements & Simulations, 5 rue du Général Cassagnou, BP 70034, 68301 Saint-Louis Cedex, France / flavien.denis@isl.eu (corresponding author)

†Research Scientist, Aerodynamics, Measurements & Simulations, 5 rue du Général Cassagnou, BP 70034, 68301 Saint-Louis Cedex, France / robert.hruschka@isl.eu

‡Research Engineer, Aerodynamics, Measurements & Simulations, 5 rue du Général Cassagnou, BP 70034, 68301 Saint-Louis Cedex, France / myriam.bastide@isl.eu

§Research Engineer, Aerodynamics, Measurements & Simulations, 5 rue du Général Cassagnou, BP 70034, 68301 Saint-Louis Cedex, France / berthold.sauerwein@isl.eu

¶Professor, Icube Laboratory, 2 rue Boussingault, 67000 Strasbourg, France / hoarau@unistra.fr

‖Professor, Icube Laboratory, 2 rue Boussingault, 67000 Strasbourg, France / mose@unistra.fr

$T$ = Temperature $[K]$

$u$ = Velocity $[m \cdot s^{-1}]$

$\theta$ = Angle with the model symmetry axis $[-]$

$\lambda$ = Heat conductivity $[W \cdot m^{-1} \cdot K^{-1}]$

$\rho$ = Density $[kg \cdot m^{-3}]$

Subscripts

$D$ = Model sphere diameter

$f$ = Fusion

$Ga$ = Gallium

$s$ = Sublimation or Stagnation point

$0$ = Total condition

$\infty$ = Freestream condition

Superscript

$\star$ = Dimensionless value

## I. Introduction

High enthalpy hypersonic flows are characterized by high temperatures in the shock layer, resulting in substantial heat transfer between the flow and the hypersonic object. The stagnation surfaces in particular are exposed to a large heat load, which degrades and eventually destroys them. This phenomenon is called ablation. As a sub-category, liquid ablation occurs when the metallic surface of a hypersonic object is heated beyond the melting point, being successively either advected downstream by the flow or evaporated.

The subject is of renewed interest owing to the development of new hypersonic applications involving the ablation of metallic parts, such as the disintegration prediction of end-of-life LEO satellites and space debris into the atmosphere ([1], [2] and [3]) and the design of hypersonic projectiles accelerated by rail-gun-launchers [4]. Moreover, liquid ablation is also relevant for the modelling of meteorite atmospheric entry.

In the present study, liquid ablation, i.e. ablation by melting is investigated. This fundamentally differs from the ablation by pyrolysis and gas blowing, which occurs for example on the heat-shields of re-entry-vehicles. Liquid ablation consists of two distinct phases: a heating phase during which the surface heats up from the initial temperature to the melting temperature and a successive melting phase. Also, a thin liquid layer develops along the body surface, which is sheared off by the flow. Thus, over time, this type of ablation leads to an important mass loss and a significant surface shape change, which in turn changes the overall aerodynamics of the object and may finally destroy it. Secondary phenomena, such as surface oxidation and radiative heat transfer can also influence the speed of the ablation process.

Most of the experimental data for liquid ablation have been obtained in the 1950s and 1960s, when metallic thermal protection systems were investigated ([5], [6] and [7]). Today, arcjet facilities are usually used for experimental studies of ablation. While they are well suited for material analysis under stagnation point flow conditions, they are not able to reproduce the aerothermodynamics experienced by a hypersonic model. However, some recent ablation experiments were carried out in hypersonic shock tunnels but they used low temperature ablators such as water ice [8] or dry ice [9] instead of an ablating metal.

Here, we present a new experimental method suitable to quantify liquid ablation of a metallic ablator that is purely melting under realistic flow conditions by using a hypersonic high-enthalpy shock tunnel.

## II. Experimental procedure

### A. Hypersonic facility

The ablation experiments are conducted within the ISL hypersonic high-enthalpy shock tunnel STB shown in Figure 1. The high-pressure part is 2.5m and the driven part 18.4m long. The inner diameter is 100mm for both parts. The facility is described in more details in [10]. For this study, the hypersonic flow is generated by expanding the test gas in a Mach 4.5 contoured nozzle. Nitrogen is used as test gas in order to avoid interference by oxidation on the ablation process. The dissociation of molecular nitrogen is negligible since the maximum stagnation temperature is below 1600K. Therefore, the model ablation is expected to be solely a combination of material melting and erosion.

Four flow conditions, summarized in Table 1 are tested. The freestream conditions are computed from the following experimentally measured parameters: the initial driver and test gas pressures, the shock propagation velocity in the shock tube and the stagnation pressure after shock reflection at the nozzle throat. The steady flow duration for these conditions is about two milliseconds, during which the stagnation pressure varies by 15 %. For all flow conditions the Knudsen number is lower than 0.03, so that the flow can be considered as a continuum flow without surface slip [11]. Due to the combination of the noisy shock tunnel flow and the freestream Reynolds number [12], the boundary layer is expected to become turbulent in the vicinity of the stagnation point region.

In the measurement section, the model is mounted 65mm downstream of the nozzle. Two side windows allow optical access for model illumination and image recording. Before the test, the pressure in the measurement section is about 5Pa.

### B. Low temperature ablating metal

Due to the short steady flow duration of only two milliseconds, metals commonly used for aerospace applications such as steel or titanium cannot be used in this ablation study, as they do not have enough time to melt. For this reason, a low-temperature ablation material has to be used. Materials used in previous studies are not well-suited for liquid ablation experiments in shock tunnels. Naphthalene [13] and camphor [14] are ablated by sublimation, while models

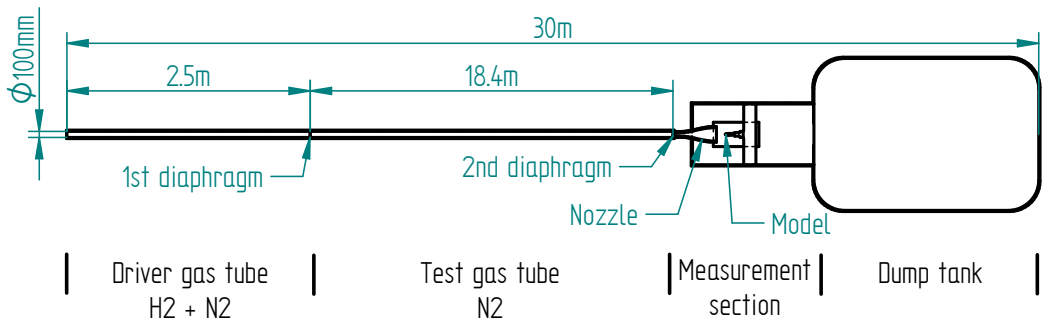


**Fig. 1 Schematic of the ISL shock tunnel**

**Table 1 Flow conditions**

| Condition n° | $M_\infty$ (-) | $Re/x$ $(m^{-1})$ | $u_\infty$ $(m \cdot s^{-1})$ | $T_\infty$ $(K)$ | $P_\infty$ $(Pa)$ | $T_0$ $(K)$ | $h_0$ $(J \cdot kg^{-1})$ | $P_0$ $(W \cdot m^{-2})$ |
|---|---|---|---|---|---|---|---|---|
| 1 | 4.43 | 4.95 E+7 | 1670 | 343 | 6.94 E+4 | 1450 | 1.76 E+6 | 2.00 E+9 |
| 2 | 4.51 | 9.06 E+7 | 1500 | 265 | 9.00 E+4 | 1160 | 1.40 E+6 | 2.40 E+9 |
| 3 | 4.53 | 5.86 E+7 | 1440 | 244 | 5.20 E+4 | 1070 | 1.29 E+6 | 1.34 E+9 |
| 4 | 4.51 | 1.73 E+7 | 1460 | 252 | 1.61 E+4 | 1090 | 1.32 E+6 | 4.15 E+8 |

made of water ice [8] or CO2 ice [9] melt and also evaporate during the test preparation.

Gallium has been chosen as substitute ablation material for the following reasons. It is a grey, non-toxic metal with a low melting temperature of 302.9K and a high boiling point of 2477K, so a purely liquid ablation can be expected during the test. Gallium properties at $10^5$Pa are given in Table 2. No significant difference to these values is observed at lower pressures. As is the case for other metals, a thin oxide layer covers the surface of the gallium model. Despite a high melting temperature of 2070K for the gallium oxide $\beta$-$Ga_2O_3$ [15], the experiments described later demonstrate that the oxide layer has a minor influence on the ablation process and is quickly stripped off by the flow.

With the exception of its low melting point, the thermal properties of gallium are of the same order of magnitude as those of other commonly used metals. The gallium ablation process can thus be considered similar to theirs.

**Table 2 Gallium properties for the solid phase (from [16] and [17])**

| $\rho_{Ga}$ $(kg \cdot m^{-3})$ | $Cp_{Ga}$ $(J \cdot kg^{-1} \cdot K^{-1})$ | $\lambda_{Ga}$ $(W \cdot m^{-1} \cdot K^{-1})$ | $\Delta H_{f,Ga}$ $(J \cdot kg^{-1})$ | $T_{f,Ga}$ $(K)$ | $T_{s,Ga}$ $(K)$ |
|---|---|---|---|---|---|
| 5904 | 370 | 41 | 80200 | 302.9 | 2477 |

### C. Model geometry

Three model geometries are used for the experiments: an 8mm-hemisphere-cone-cylinder, a 10mm-hemisphere-cone-cylinder and a 14mm-hemisphere-cylinder, which are mounted on a rearward-facing sting. Due to the short duration of the experiment, the heating is expected to occur exclusively within the model. The geometries with their dimensions are shown in Figure 2.

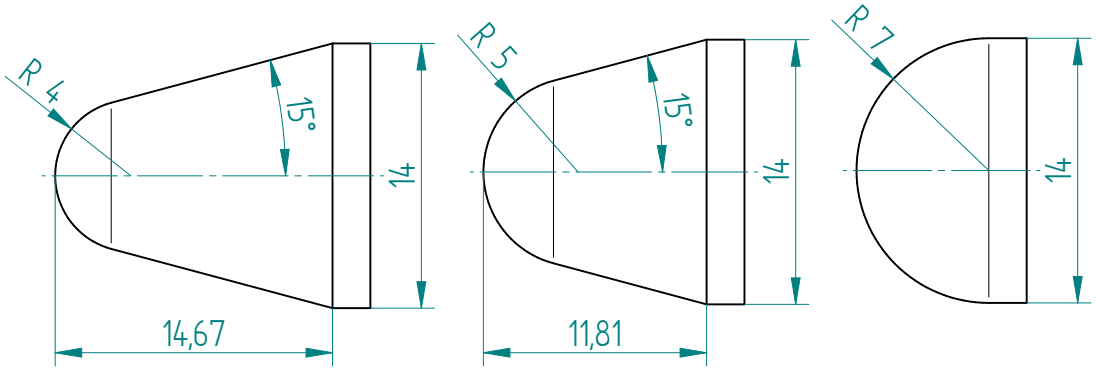


**Fig. 2 8mm-, 10mm- and 14mm-hemisphere-cylinder geometries**

Due to the low melting temperature of gallium the model cannot be machined. Thus a custom model generation technique based on low temperature casting has been developed. First, gallium is melted and heated up to 333K. At the same time, the 3D-printed molds are assembled on the model sting and preheated to 333K for 15min. Then the liquid gallium is cast into the molds and left to cool down at ambient temperature during 15min. Thereafter, the model is cooled down to near 273K until the gallium solidifies. Finally, the molds are removed and the model is polished before being used in the experiment. This procedure ensures that the model is free of blowholes and is mechanically smooth. Pictures of the model production tools are presented in Figure 3.

A summary of the performed runs with the corresponding Reynolds number is given in Table 3.

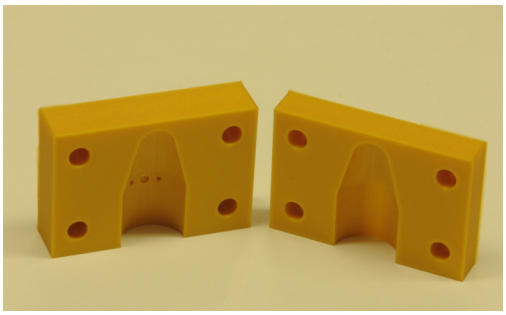

**(a) 3D-printed molds**

**(b) Molds/sting casting assembly**

**Fig. 3 Model generation tools**

**Table 3 Test summary**

| Condition n° | Model geometry | Number of runs | $Re_D$ |
|---|---|---|---|
| 1 | Hemisphere Ø8mm-cone | 6 | 3.96 E+5 |
| 1 | Hemisphere Ø10mm-cone | 8 | 4.95 E+5 |
| 1 | Hemisphere Ø14mm-cylindre | 6 | 6.92 E+5 |
| 2 | Hemisphere Ø10mm-cone | 2 | 9.06 E+5 |
| 3 | Hemisphere Ø10mm-cone | 3 | 5.86 E+5 |
| 4 | Hemisphere Ø10mm-cone | 3 | 1.73 E+5 |

### D. Optical set-up

A direct visualization system, as schematically shown in Figure 4, is applied for accurate model position and surface recession tracking without any interference by light refraction induced by the bow shock wave. The light source consists of a 6kJ flash lamp illuminating a diffuser, which provides nearly constant background illumination for as much as 10ms.

Two high speed cameras Photron SA-X record the test at 12500 frames per second with an exposure time of 0.293µs, ensuring negligible motion blur. Using a beam splitter and two different camera lenses, different magnification levels for each camera are achieved. The first camera records a low magnified image of the model with a first camera lens of 300mm focal length combined with a 1.4 extender placed before the beam splitter. The second camera records a highly magnified image through an additional camera lens of 105mm focal length. With this setup, both cameras share the same line of sight with the approximate magnifications of 0.02mm/px for the first and 0.005mm/px for the second. The exact magnifications are measured before each test, as they are further required for the image post-processing.

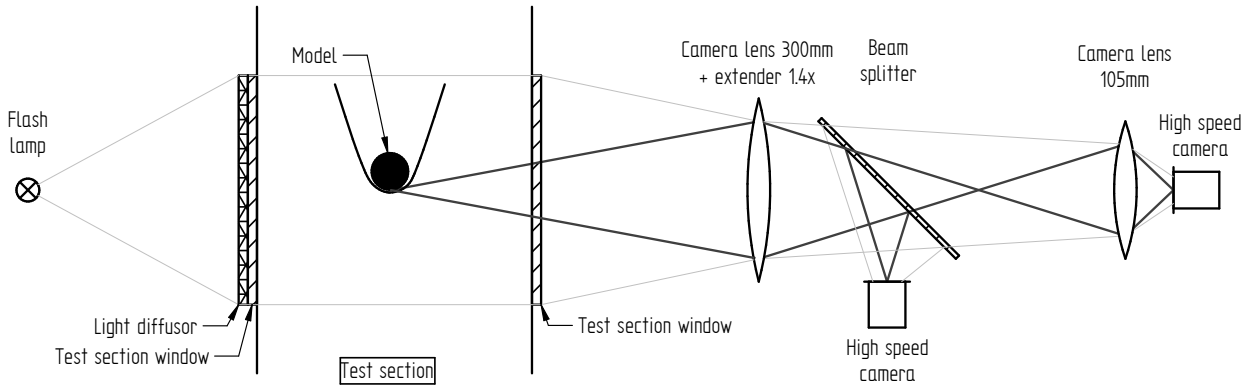


**Fig. 4 Optical setup**

## III. Image processing algorithm

During the test, the model vibrates and the ablation trails hide parts of the model surface, requiring image post-treatment before the ablation profile extraction. The main steps of this process are shown in Figure 5.

First, one reference image is selected for each magnification level, taken at the same time when the flow is established but the ablation process is not started yet. The model profile extracted corresponds to the initial state of the ablation profiles.

The displacement of the model caused by sting vibration is tracked for each frame of the low-magnification video using a cross-correlation with the reference image. The obtained correction for vibration is then applied to both video recordings, taking into account the magnification ratio.

Before model surface contour extraction, each frame is normalized by applying a median blur, a gray scale dilation and a threshold. The ablation profiles are computed by determining the local minimum distance between the reference image contour and the actual frame contour.

The post-treatment uncertainty is one pixel when the surface visualization is undisturbed. It is determined by applying the post-treatment algorithm to a non-ablative model. During the test, ablation trails flow around the model and partially shroud the model surface, inducing some additional error in the model vibration correction and consequently in the calculation of the ablation profiles. To compensate for this uncertainty, the ablation profiles shown in the following sections are temporally averaged over seven consecutive frames. Additionally, they are spatially averaged, retaining a resolution of 0.05mm.

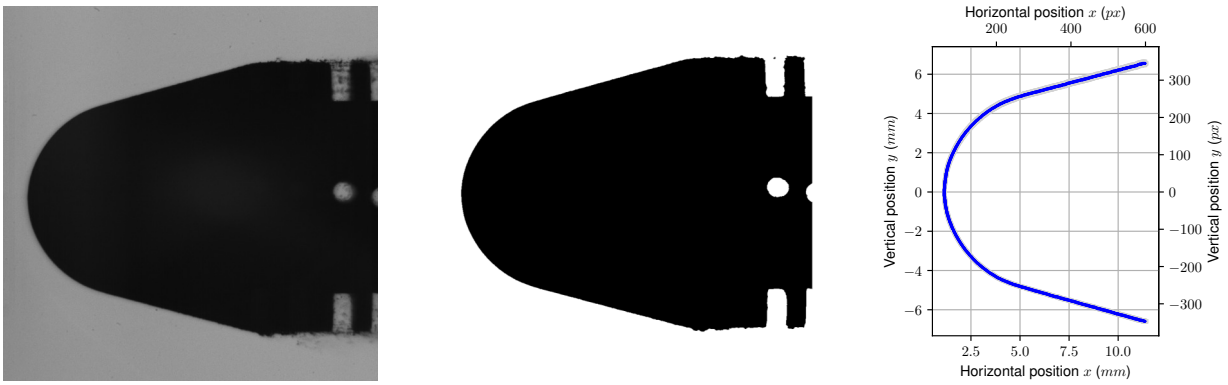


**(a) Raw image** **(b) Normalized image** **(c) Extracted contour**

**Fig. 5 Images from the post-processing**

## IV. Experimental results and discussion

### A. Qualitative description

Ablation is observed for all flow conditions and for all models, primarily in the vicinity of the stagnation point region on the hemispherical part. The generated liquid layer is then sheared off along the model surface by the flow. No ablation by erosion was observable in any video, confirming that the main ablation process in this experiment is ablation by melting.

The model images presented in Figure 6 do not show the ablated region but rather the region affected by the liquid layer, which re-solidified once the steady flow had passed. They do, however, provide a first indicator of the ablation intensity. As expected, the ablation is most significant at the conditions with the highest flow enthalpy, namely flow conditions 1 and 2. For condition 4, on the contrary, the region contaminated by the re-solidified ablation layer is restricted to the model hemisphere only, thus indicating only weak ablation.

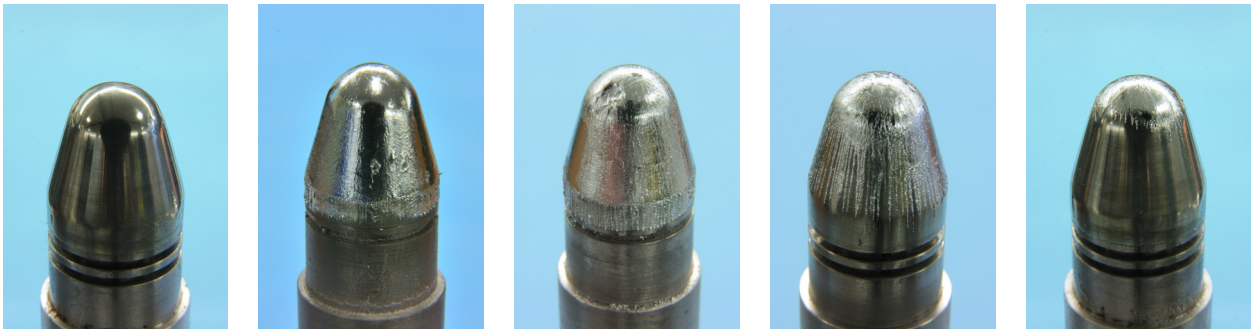

**(a) Before testing** **(b) Condition 1** **(c) Condition 2** **(d) Condition 3** **(e) Condition 4**

**Fig. 6 10mm-hemisphere-cone models before and after testing**

### B. Effect of the flow condition on the heating phase duration

The heating phase duration is defined as the period between the steady flow establishment and the ablation start. During this phase the model wall temperature increases from the initial temperature to the melting temperature of the material.

The heating phase durations extracted from the test videos are presented in Table 4. The measurement uncertainty is about 0.2ms. It is mainly caused by the uncertainty in the nozzle steady flow starting point. For the high enthalpy conditions 1 and 2, the ablation starts earlier compared to the lower enthalpy conditions due to the increased surface heat transfer. The differences in the measured ablation start times for the high enthalpy conditions 1 and 2 are within the measurement uncertainty, so that no conclusion can be drawn regarding the dependencies on the model diameter or on the flow parameters.

**Table 4 Heating phase durations**

| Condition n° | Model geometry | Heating phase duration (*ms*) |
|---|---|---|
| 1 | Hemisphere Ø8mm-cone | 0.5 |
| 1 | Hemisphere Ø10mm-cone | 0.5 |
| 1 | Hemisphere Ø14mm-cylindre | 0.4 |
| 2 | Hemisphere Ø10mm-cone | 0.4 |
| 3 | Hemisphere Ø10mm-cone | 0.9 |
| 4 | Hemisphere Ø10mm-cone | n/a |

### C. Ablation profiles as a function of time

The present method allows the tracking of the ablation profiles as a function of time for the high enthalpy flow cases.

An example of ablation profiles as a function of time is given in Figure 7. At the early phase of ablation the measured profile is somewhat asymmetric. From 1.5ms onwards, the profile asymmetry is less pronounced. Even though some local asymmetries remain, the observations show that the ablation globally preserved the model symmetry. It is to note that the ablation profile at 0ms is not zero for all angles, as it is time-averaged over seven frames and also the model already vibrates before the nozzle flow is established, causing some position uncertainty.

It can be observed that from the ablation start time onwards the profiles are similar in their overall shape, featuring two local maximums: the first located at the stagnation point and the second near 20°-40°. These maximums are even more pronounced at 2ms. Similar ablation profiles were observed on water ice models in supersonic wind tunnel tests [8] as well as on aluminium spheres in a ballistic hypersonic free flight tunnel [7]. In these experiments, the location for maximum ablation was related to the position of the laminar-turbulent transition of the boundary layer.

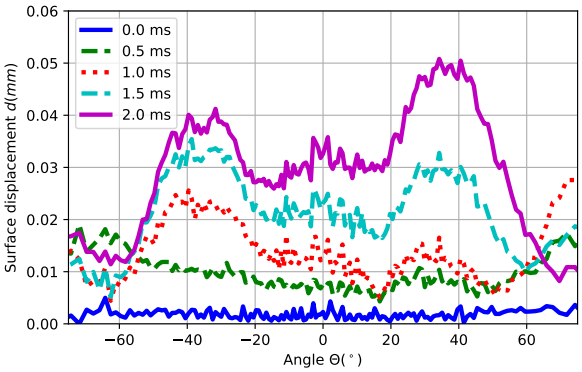


**Fig. 7 Ablation profiles for the 8mm-hemisphere at the flow condition 1**

### D. Effect of the hemisphere diameter on the ablation profiles

The ablation profiles obtained at 2ms at flow condition 1 for the three different hemispheres are presented in Figure 8. Despite some scattering in the data and a surface displacement of less than 0.1mm, the characteristic ablated shapes with the two ablation maxima are clearly observable for each tested geometry.

The first ablation maximum is located at the stagnation point, where the laminar wall heat flux is maximal. The second ablation maximum corresponds to the position of maximal ablation and is always observed near 30° from the symmetry axis. The higher ablation rate results from an increase in the melting rate due to an increasing wall heat flux caused by the boundary layer transition. The Reynolds number regime and the noisy shock tunnel flow suggest that the boundary layer may become turbulent somewhere along the hemisphere surface. This would lead to an increase in wall heat flux just downstream of the laminar-turbulent transition. Following this hypothesis, the position of the

ablation maximum should also depend on the model hemisphere diameter. However, this location shift is too small to be observed within the scatter of the data, i.e. it is within the measurement uncertainty.

What can be observed in Figure 9a, however, is a shift of the ablation local minimum located between 10° and 20°. It is shifted from 15°-20° for the 8mm-hemisphere to 10° for the 14mm-hemiphere, thus it is in agreement with the expected direction of the displacement of the laminar-turbulent transition. It should be noted that the ablation profiles are similar irrespective of the hemisphere diameter. Therefore and by also considering the measurement uncertainty, no conclusion can be drawn regarding the dependency of the magnitude of ablation on the hemisphere diameter.

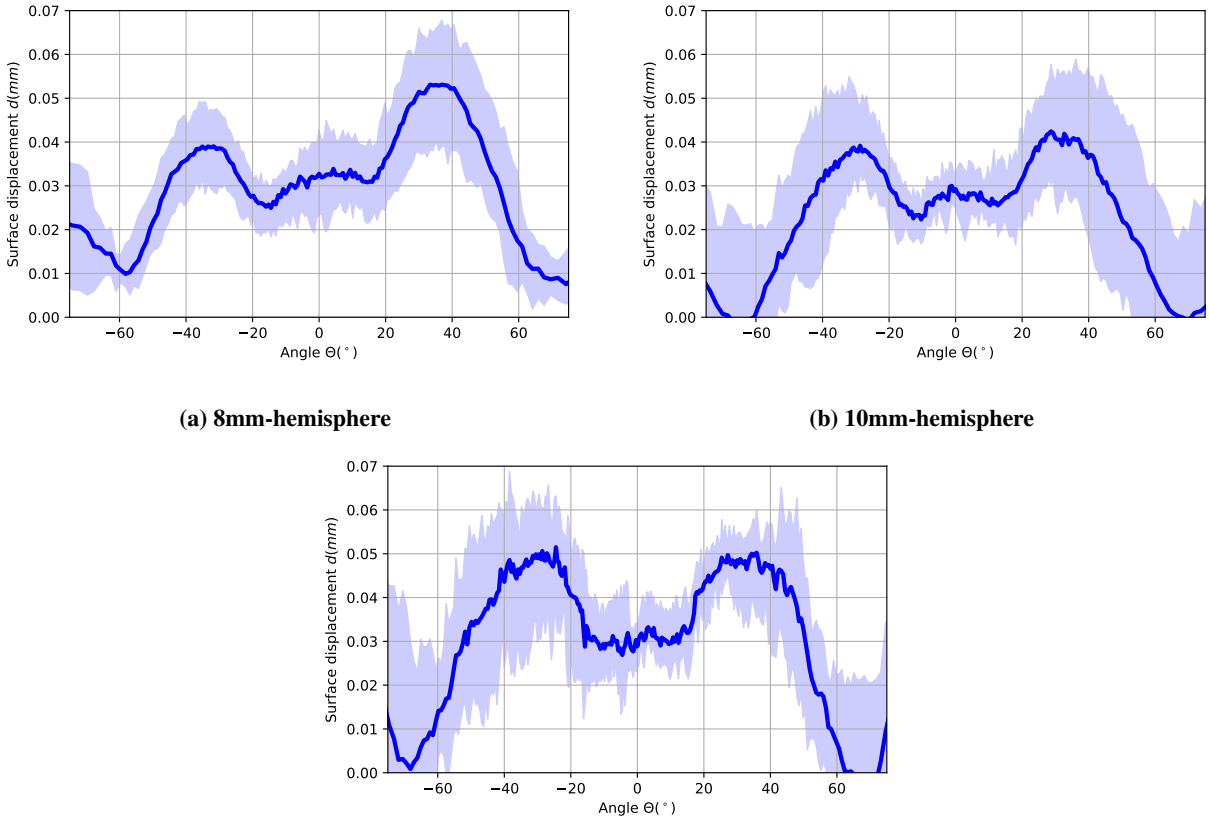


**(a) 8mm-hemisphere**

**(b) 10mm-hemisphere**

**(c) 14mm-hemiphere**

**Fig. 8 Ablation profiles at $t = 2ms$ for condition 1 with the uncertainties represented by the blue areas**

### E. Ablation profiles as a function of the flow conditions

The dependency of the ablation profiles on the flow condition are presented in Figure 9b for the 10mm-hemisphere-cone model. While the low enthalpy condition 4 leads to no measurable ablation, the comparisons of flow conditions 1 and 2 clearly show the same trend. Due to frequent impacts of shock tunnel membrane debris on the model, only two valid ablation measurements are available for condition 2. So, for a better comparability, the surface displacement $d$ is normalized by the surface displacement at the stagnation point $d_s$, yielding $d^*$:

$$d^* = \frac{d}{d_s} \tag{1}$$

The ablation profiles for condition 2 are similar in shape with the two ablation maxima located at nearly the same position on the hemisphere, thus suggesting no change in the overall physics of the ablation process. The scattering in the data prevents the determination of the precise location in the ablation minima and maxima, making it impossible to verify the aforementioned hypothesis of a transition-related shift of maximum ablation.

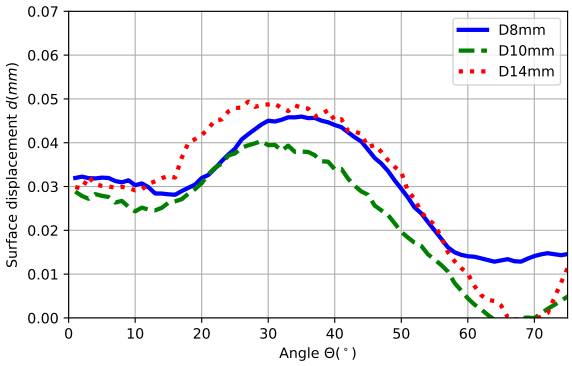


**(a) Ablation profiles for 3 model diameters at condition 1**

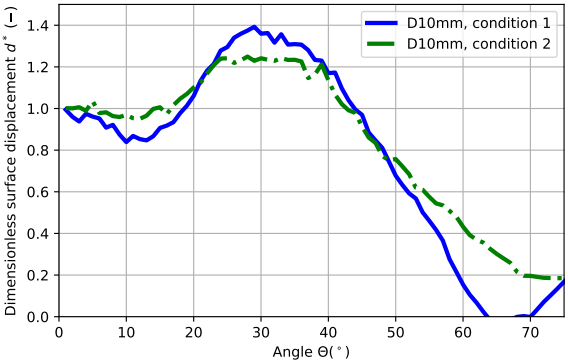


**(b) Dimensionless ablation profiles for 2 flow conditions and for the 10mm-hemisphere-cone**

**Fig. 9 Comparison of ablation profiles at $t = 2ms$**

## V. Conclusion

Using a hypersonic shock tunnel facility, a new experimental method for quantitative ablation rate measurements under realistic flow conditions in terms of Mach and Reynolds numbers is presented. The use of gallium as low melting point metal allows to measure ablation profiles within less than 2ms. Gallium as a substitute ablator is chosen, since its ablation behaviour is similar to other metals classically used in aerospace applications. The surface displacement is determined with a combination of a direct visualization system and an image processing algorithm, allowing surface displacements caused by ablation of less than 0.1mm to be detected.

Quantitative measurements are only possible for high-enthalpy flow conditions when the ablation rate is high enough. Uncertainties due to measurement scatter remain high but are reduced by performing multiple runs.

The ablation profiles obtained with this method show similarities with previous observations made using different facilities. The ablation maximum is never located at the stagnation point but at a location near 30° from the symmetry axis. The proposed explanation is that the boundary layer becomes turbulent just upstream of this position and increases the local wall heat flux, enhancing the ablation process.

Finally, we described a new measurement method able to investigate the liquid ablation phenomena under realistic

flow conditions in terms of Mach and Reynolds numbers. The method has the potential to enhance the database for ablation for hypersonic dense flows, which can be used for the validation of a future CFD solver dedicated to the simulation of liquid ablation.

## Funding Source

This work is funded by the French-German Research Institute of Saint-Louis.

## Acknowledgments

This work is supported in the framework of a Ph.D. thesis by the French-German Research Institute of Saint-Louis, the Icube Laboratory (UMR7357) of Strasbourg University and the doctoral school 269 Mathematics, Sciences of the Information and the Engineer of Strasbourg. The authors gratefully acknowledge the technical support of Robert BERNHARD, Remy KEMPF, Kevin MARTINEK and Jean-Marc WUNDERLY.

## References

[1] United Nations - Office for Outer Space Affairs, "Space debris mitigation guidelines of the Committee on the peaceful uses of outer space," 2010.

[2] Grassi, L., Bianchi, S., Destefanis, R., Kanzler, R., Bassaler, P., and Heinrich, S., "Design for demise techniques for medium/Large LEO satellites reentry," *7th European Conference on Space Debris, ESA*, 2017.

[3] Annaloro, J., Galera, S., Karrang, P., Prevereaud, Y., Verant, J., Spel, M., Van Hauwaert, P., and Omaly, P., "Space debris atmospheric entry prediction with spacecraft-oriented tools," *7th European Conference on Space Debris, ESA*, 2017.

[4] Hundertmark, S. and Lancelle, D., "A scenario for a future European shipboard railgun," *IEEE Transactions on Plasma Science*, Vol. 43, No. 5, 2015, pp. 1194–1197, https://doi.org/10.1109/TPS.2015.2403863.

[5] Bridges, J. and Pinchok, R., "An experimental investigation of the re-entry behavior of metals and alloys," *Westinghouse Astronuclear Laboratory*, 1964.

[6] Chang, P. K., "Analysis of the aerodynamic ablation of a metal sphere," *Naval Research Lab Washington DC*, 1963.

[7] Luneau, J., "Contribution à l'étude des phénomènes aérothermiques liés au vol hypersonique décéléré (in French)," *Institut franco-allemand de recherches de Saint-Louis*, 1969.

[8] Silton, S. I. and Goldstein, D. B., "Ablation onset in unsteady hypersonic flow about nose tip with cavity," *Journal of thermophysics and heat transfer*, Vol. 14, No. 3, 2000, pp. 421–434, https://doi.org/10.2514/2.6540.

[9] Callaway, D., Reeder, M., Greendyke, R., and Gosse, R., "Photogrammetric measurement of recession rates of low temperature ablators in supersonic flow," *48th AIAA Aerospace Sciences Meeting*, 2010.

[10] Gnemmi, P., Srulijes, J., Seiler, F., Sauerwein, B., Bastide, M., Rey, C., Wey, P., Martinez, B., Albers, H., Schlöffel, G., Hruschka, R., and Gauthier, T., "Shock tunnels at ISL," *Experimental Methods of Shock Wave Research*, 2016.

[11] Moss, J. N. and Bird, G. A., "Direct simulation of transitional flow for hypersonic reentry conditions," *Journal of spacecraft and rockets*, Vol. 40, No. 5, 2003, pp. 830–843, https://doi.org/10.2514/2.6909.

[12] Oertel, H., "Strömungsmechanik: Methoden und Phänomene (in German)," *Springer-Lehrbuch*, 1995.

[13] Combs, C. S., Clemens, N. T., Danehy, P. M., and Murman, S. M., "Heat-shield ablation visualized using naphthalene planar laser-induced fluorescence," *Journal of Spacecraft and Rockets*, Vol. 54, No. 2, 2017, pp. 476–494, https://doi.org/10.2514/1.A33669.

[14] Stock, H. W. and Ginoux, J. J., "Hypersonic low temperature ablation an experimental study of cross-hatched surface patterns," *Astronautical Research 1971, Springer*, 1973, pp. 105–120.

[15] Víllora, E. G., Shimamura, K., Yoshikawa, Y., Ujiie, T., and Aoki, K., "Electrical conductivity and carrier concentration control in $\beta$-Ga2O3 by Si doping," *Applied Physics Letters*, Vol. 92, 202120, No. 20, 2008, https://doi.org/10.1063/1.2919728.

[16] NIST-JANAF, "Thermochemical tables, Gallium (Ga)," 1998.

[17] Ayrinhac, S., "Compilation of thermodynamic and elastic data of liquid Ga," *UPMC, Sorbonne Universités*, 2000.